# Numerical modeling of tidal propagation and frequency responses in the Guadalquivir estuary (SW, Iberian Peninsula)

P. Muñoz-Lopez [a,b,*], I. Nadal [a,b], J. García-Lafuente [a,b], S. Sammartino [a,b,c], A. Bejarano [d]

[a] *Physical Oceanography Group, Department of Applied Physics II, University of Málaga, Málaga, Spain*
[b] *Instituto de Biotecnología y Desarrollo Azul (IBYDA), University of Málaga, Málaga, Spain*
[c] *Instituto de Ingeniería Oceánica (IIO), University of Málaga, Málaga, Spain*
[d] *Port Authority of Seville, Seville, Spain*

ARTICLE INFO

ABSTRACT

A three-dimensional numerical model, based on Delft3D code, has been implemented and calibrated in the mesotidal Guadalquivir Estuary (Spain), a tidally-driven estuary due to the reduced freshwater discharges (25 $m^3s^{-1}$ year-round average), which are subject to human regulation at the dam located at its head. The model has been applied to study in detail some estuarine features for low freshwater discharges: the first one is the non-linear interaction of semidiurnal constituents, which results in a tidal amplification factor (ratio of local amplitude to the amplitude at the mouth) that depends on the spring-neap tidal cycle, with markedly larger values during neap tides. The second one is the analysis of tidal resonance in the estuary, extending previous studies on the topic, which shows that resonance occurs at near-diurnal frequencies. The peak of resonance decreases in magnitude and shifts towards lower frequencies as friction increases, either by increasing the friction coefficient itself or the amplitude of the tide.

## 1. Introduction

The Guadalquivir Estuary (GE, hereinafter), where the Guadalquivir River meets the Gulf of Cádiz in the Atlantic Ocean (Fig. 1a), is a relevant and anthropogenized coastal system of the Iberian Peninsula (Ruiz et al., 2015). It extends from Sanlúcar de Barrameda to Alcalá del Río dam, located ~110 km upstream from the river mouth, and is navigable up to Seville harbor, located ~80 km inland (Fig. 1b), with an average width of ~360 m. The estuary is a human-mediated navigation channel of smooth bathymetric variations with a mean water depth of 6.5 m (Donázar-Aramendía et al., 2018), which is maintained by periodic dredging works carried out by the Port Authority of Seville when necessary.

The primary driving force of GE dynamics is the oceanic tide at the mouth (Álvarez et al., 2001; Díez-Minguito et al., 2012a). The so-called meteorological tide (and eventual storm-surges in the Gulf of Cádiz) and freshwater discharges at different upstream locations are minor drivers that may become relevant under extreme circumstances. The primary freshwater discharge occurs at the Alcalá del Río dam, which is

human-regulated to meet the requirements of various social sectors, particularly agricultural sector due to the vast rice field extensions located in the middle stretch. The year-averaged discharge is around 25 $m^3/s$, being less than 40 $m^3/s$ for over 75% of the time (Bermúdez et al., 2021) and, paradoxically, above the average in summer, the driest season, due to the irrigation of rice crops. Such low discharges result in a clearly tidally-driven and well-mixed estuary (Díez-Minguito et al., 2012a). The tide is largely semidiurnal, the major tidal constituent being $M_2$ (principal lunar) with amplitude of around 1 m near Cádiz (García-Lafuente et al., 2012), followed by $S_2$ (principal solar), $N_2$ (larger lunar elliptic), and $K_2$ (luni-solar semidiurnal). Diurnal constituents $K_1$ (luni-solar diurnal) and $O_1$ (principal diurnal) have amplitudes an order of magnitude less than $M_2$ and are of minor significance.

A relevant feature of the GE is the tidal reflection at the Alcalá del Río dam at the estuary's head (Fig. 1b). The dam makes a difference with another nearby meso-tidal Atlantic estuaries of the Iberian Peninsula, such as the Guadiana River, that shares tidal propagation features with the GE (southwestern Spain; Garel and Cai, 2018) or the Tagus Estuary (Dias et al., 2013). Tidal dynamics in the GE was extensively

---

investigated by Díez-Minguito et al. (2012a,b) using water-level data collected from June to December 2008. According to these authors, the estuary is divided into three stretches controlled by different tidal processes. Near the mouth, bottom friction overcomes inertial acceleration and causes a decrease of tidal amplitude, which is quantitatively described using a diffusion equation for elevations proposed by Díez-Minguito et al. (2012a). In the middle part, balance between friction and channel convergence results in a synchronous behavior (Díez-Minguito et al., 2012a), whereas in the upper stretch the tide is the superposition of an incident and a reflected wave at the dam (Díez-Minguito et al., 2012b; Cai et al., 2016, 2018) that gives rise to a quasi-standing wave pattern with tidal amplitude increasing again landwards. This phenomenon is not observed in other parts of the estuary, although the superposition still results in an amplitude minimum in the middle of the estuary, which has been defined as a virtual node by Cai et al. (2016). The antinode, on the other hand, is located at the closed end where the amplitude reaches its maximum and the velocity is null.

Studies addressing tidal dynamics, frequency response and interaction between tidal constituents in the GE have been carried out from different approaches, including analytical models (Cai et al., 2018). Barotropic 1D and 2D numerical models have been also applied (Cai et al., 2018; Siles-Ajamil et al., 2019; Gomiz-Pascual et al., 2021) to explain the key features of the tidal dynamics in the estuary. These numerical approaches, endorsed by the vertically mixed nature of the estuary, reproduce satisfactorily the tidal response derived from observations, although small local discrepancies may be noticed. The application of a full 3D model that accounts for the baroclinic nature of the estuary is the obvious next step, which is addressed in the present study. It has the double objective of presenting the most complete 3D numerical model implemented in the GE so far and to apply the model to investigate relevant aspects of the tidal fortnightly variability arising from the interaction of individual tidal constituents, and the resonance response of the estuary. Section 2 describe the hydrodynamic model, the initial and boundary conditions and the calibration parameters (specific details about grid model and tidal forcing are presented in Appendices A1 and A2). The validation is addressed in Section 3 (the available observations for calibration are shown in Appendix A3). Section 4 presents the tidal forcing scenarios that correspond to the different case studies investigated in the following sections and the procedure followed to define them. Section 5 investigate the interactions of tidal constituent (in low river freshwater discharges) and some peculiarities of spring and neap tidal cycles. Section 6 addresses the frequency response of the tide in the estuary and the role of friction. Section 7 discusses the findings of the study, and finally, Section 8 summarises the conclusions.

## 2. Numerical model

### 2.1. Model domain

The numerical model is the Delft3D-Flow model, which is a 3D finite-difference hydrodynamic code developed by WL|Deltares (formerly Delft Hydraulics) in collaboration with Delft University of Technology. Delft3D is an open-source modeling package consisting of several modules, connected over a mutual interface (Parsapour-Moghaddam and Rennie, 2017), that solve the baroclinic Navier-Stokes and transport
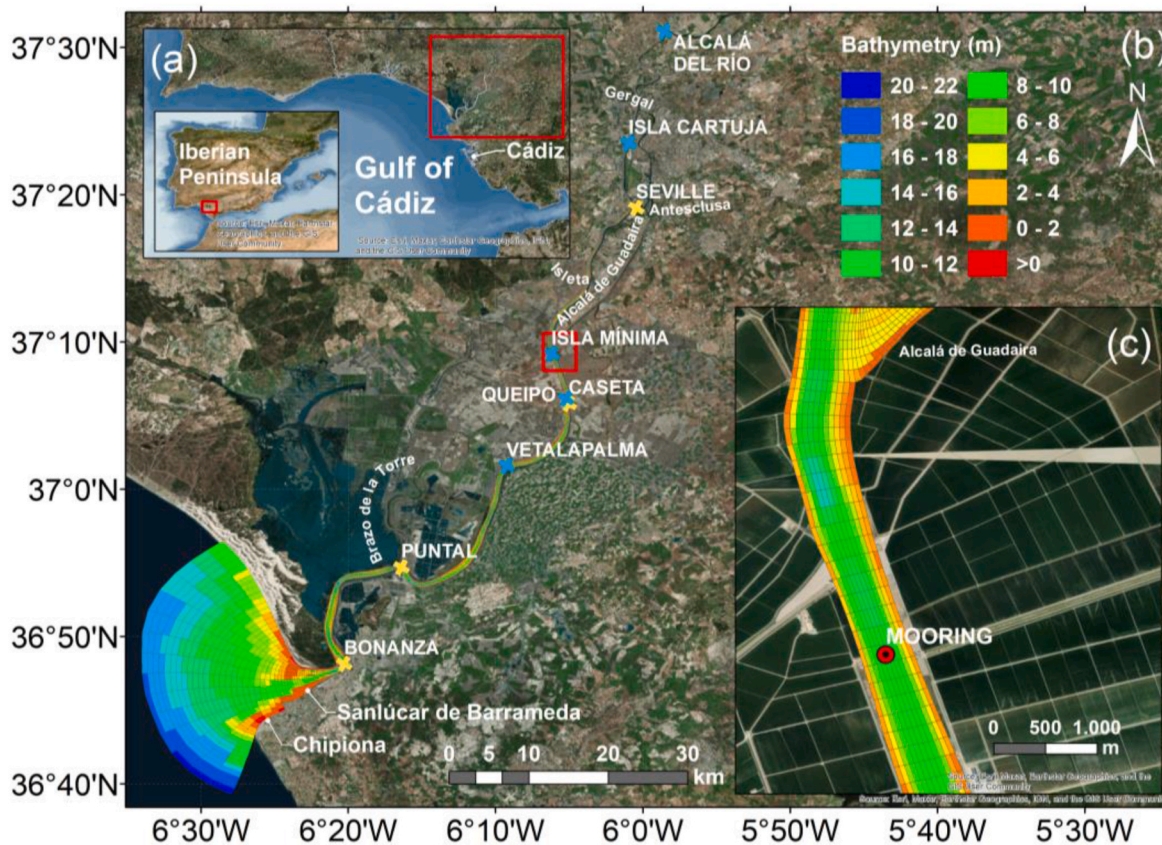


**Fig. 1.** (a) Map covering the north-central Atlantic Ocean and Western Mediterranean Sea, showing the location of the GE (red square) in the Iberian Peninsula. (b) Map of the GE showing the model domain, bathymetry, tributaries and tide-gauge stations used for validation: blue crosses are Guadalquivir Hydrographic Confederation stations and yellow crosses "Puertos del Estado" (Spanish National Port Authority) stations. (c) Zoom of the model domain displaying the junction of the main channel and Alcalá de Guadaira tributary (white rectangle in panel b). Red circle indicates the location of the current profiler mooring, which is also used for validation. Maps were created using ArcMap™ software (v. 10.8) of ArcGIS® (https://www.arcgis.com/), that are intellectual property of Esri and are used herein under license.

equations under the Boussinesq approximation for incompressible fluids. The formulation is described in detail by Lesser et al. (2004) and the source code and documentation are freely available at Deltares (2022).

The domain of the model extends from $5° 58'$ W to $6° 34'$ W and from $36° 39'$ N to $37° 31'$ N (refer to Fig. 1b) and it is discretized by a curvilinear orthogonal grid of non-uniform resolution that follows the staggered Arakawa-C grid scheme. Bathymetry was obtained from Seville Port Authority and the Spanish Marine Hydrographic Institute. Appendix A1 gives detailed information on the domain and grid implementation.

Horizontal advection terms in momentum and transport equations were discretized using the cyclic method for shallow water equations (Stelling and Lendertse, 1991). For time discretization, an alternate-direction implicit algorithm with two different time steps per iteration is used. Water level is computed at the cell centers, while velocity components are given perpendicular to the cell faces at their centers. Turbulence is resolved using a second-order κ-ε closure model based on the eddy viscosity (Uittenbogaard et al., 1992), which was refined by applying horizontal and vertical Forester filters (Forester, 1979) to remove computational noise.

### 2.2. Initial and boundary conditions

The model is initialized with zero velocity and flat free-surface. Astronomical tide is prescribed at the ocean boundary via sea level oscillation created by 27 tidal constituents, whose amplitudes and phases have been obtained from the nearby port of Cádiz (García-Lafuente, 1986). Small spatial variations of the harmonic constants over the 30–40 km distance between Cádiz and the model boundary (Fig. 1b) are expected to occur. Therefore, their final values at the boundary have been slightly adjusted during the calibration process (see Appendix A2).

Freshwater discharges from the database of hydrological information for river flood management (SAIH, https://www.chguadalquivir.es/saih/) are prescribed as water flux conditions in the cells attached to the freshwater sources, mainly Alcalá del Río dam, which represents almost 80% of freshwater contributions in the estuary (Bermúdez et al., 2021). The model also includes secondary freshwater inputs from the tributaries (Fig. 1b).

### 2.3. Calibration parameters

Background horizontal viscosity and diffusivity were set to 1 m²s⁻¹ and 10 m²s⁻¹, respectively (Deltares, 2022). No background for vertical magnitudes was used. Bottom stress

$$\vec{\tau} = \frac{g \rho_0 \vec{u_b} |\vec{u_b}|}{C^2} \qquad [1]$$

($g$ gravity, $\rho_0$ a reference density and $u_b$ the near-bed velocity) uses the 3D version of the Chézy friction coefficient C defined through the river bed roughness length $k_s$:

$$C = \frac{\sqrt{g}}{\kappa} ln \left( 1 + 15 \frac{\Delta z_b}{k_s} \right) \qquad [2]$$

($\kappa$ the dimensionless Von Kármán constant (~0.41) and $\Delta z_b$ the bed layer thickness). Equations [1] and [2] establish direct proportionality between friction and $k_s$. The value $k_s = 1.5 \cdot 10^{-4}$ m was found to match best model outputs with observations.

Reflection parameter

$$\alpha = T_d \sqrt{\frac{H}{g}} \qquad [3]$$

specifies the degree to which a boundary condition is less reflective for short wave disturbances (Deltares, 2022). Here, $H$ is a typical depth and $T_d$ the time a disturbance takes to travel from one river bank to the other. If it travels at the long-wave speed $c = \sqrt{gH}$ and $L$ is a characteristic width, then $\alpha = L/g$ from Eq. [3]. For $L = 1200$ m, the estuary width at the mouth where reflection of short waves must be minimized, $\alpha = 122$ s², the value used in this study.

## 3. Model validation

Model validation is performed via harmonic analysis (Pawlowicz et al., 2002) by comparing harmonic constants derived from water level observations, which are specified in Appendix A3, and the model outputs (Fig. 2). It is worth highlighting some aspects of Fig. 2 revealed by the observations before making that comparison. Amplitudes of semidiurnal constituents ($M_2$, $S_2$ and $N_2$) show a V-shaped pattern, with minimum occurring by the middle of the estuary and maxima at the mouth and head, in agreement with earlier studies (Díez-Minguito et al., 2012b). However, $M_2$ reaches the absolute maximum at the head of the estuary, whereas $S_2$ and $N_2$ do it at the mouth, a dissimilarity attributed to friction in Section 5. Diurnal constituents ($O_1$, $K_1$) are much smaller, with a still weakly V-shape profile and maximum amplitude at the head. Phases increase monotonically with distance (except for $O_1$), indicating the tidal wave progression in the estuary. The phase gradient is steeper from the mouth to the location where semidiurnal amplitudes are at their minimum, indicating slower wave speed in the lower half of the estuary.

The former features are quite satisfactorily reproduced by the model. When the data quality is poor (yellow or orange symbols in Fig. 2), the derived harmonic constants differ more with those calculated from the model than when the six-month period of best observations (black symbols in Fig. 2) is used (see details about data quality in Appendix A3). The observation does not apply when data is flagged as "good-quality" (compare green and black symbols in Fig. 2). The small numbers on the x-axis represent the amplitude differences (cm) between the model and observation. For the $M_2$ component, these are clearly below 3 cm, with the exception of the central region of the GE (Caseta, Queipo), where it reaches 5.5 cm. This zone is particularly challenging due to the presence of numerous irrigation channels that take and return water to the GE and also by the shallowness of the sites where tide gauges are deployed. Data quality here is suspicious (color code in Fig. 2, see also Appendix A3). Model outputs agree better with observations when the selected grid cell used in the harmonic analysis lies in the middle of the channel instead of close to the river bank where the gauge is measuring. The model accurately replicates the continuous increase in phase from the mouth to the head of the estuary and display differences of less than 10 min (numbers on the x-axis in bottom panels of Fig. 2) for the semidiurnal constituents.

Non-linear constituent $M_4$ is not prescribed at the open boundary. It is generated by the model through friction. Its amplitude is slightly greater than that derived from observations, but the spatial patterns are similar: a steady increase up to Vetalapalma station, followed by a small flattening in the middle estuary to increase again towards the head, evidencing the cumulative influence of friction on the propagation of the tide. Phases also agree, although differences in time between observations and model (revealed by numbers on the x-axis) are somewhat higher due to the greater frequency of this constituent.

A comparison of observed and modelled water levels also shows good agreement: Pearson correlation coefficients between observed and modelled water levels at Bonanza and Seville (representative stations of the lower and upper stretch of GE) are 0.981 and 0.985, and root mean square errors (RMSE) are 1.3 cm and 1.1 cm, respectively. Velocity profiles collected at a single point located by the middle stretch of the estuary (see Fig. 1c for location and Appendix A3 for details) were also used to check the model outputs. The short duration of the campaign (two days long) does not allow for a more rigorous comparison based on harmonic analysis and only the direct visual comparison at the five levels shown in Fig. 3 is presented to support the model's good
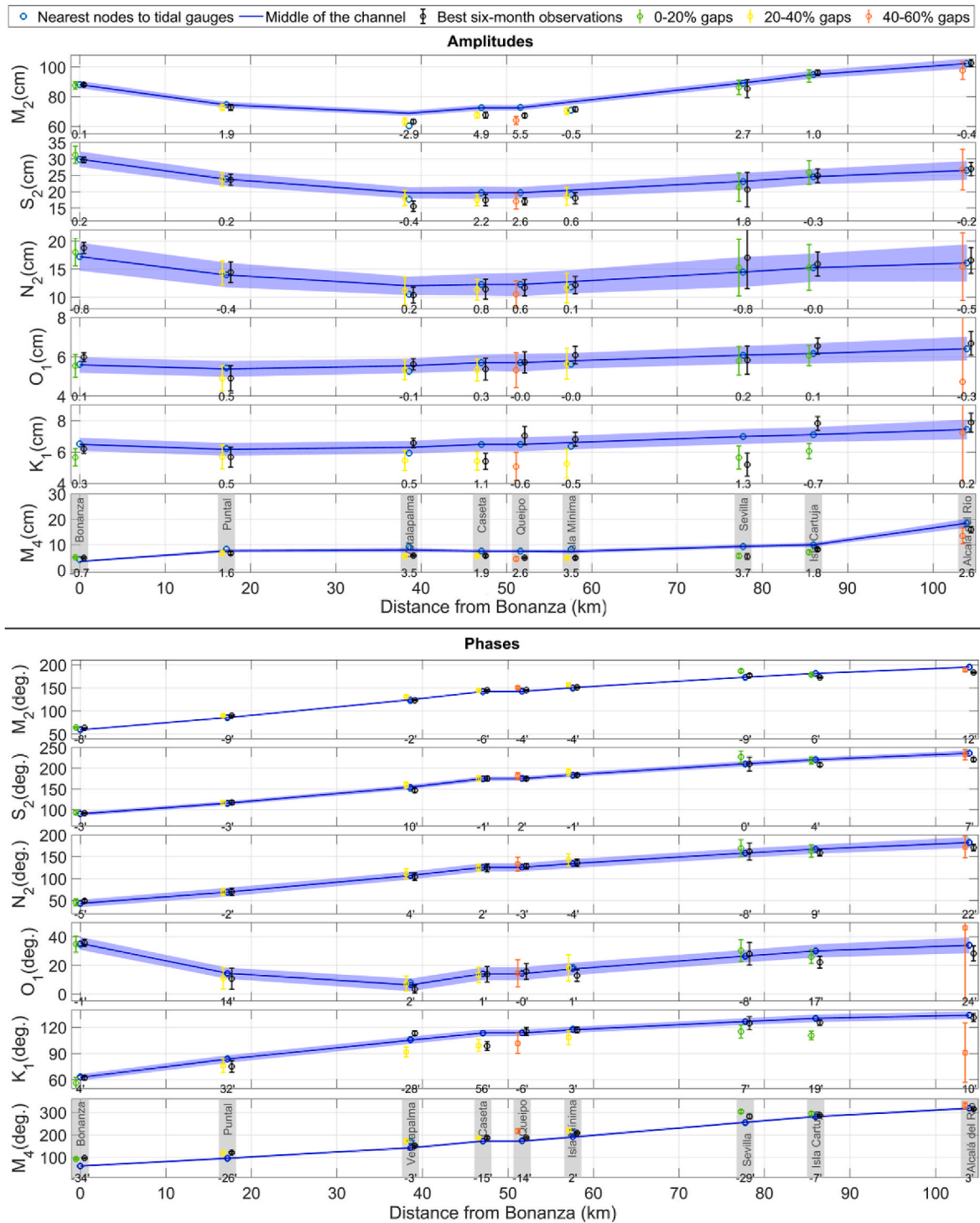
**Fig. 2.** Amplitude (cm, top block of six panels) and phase (degrees, bottom block) of six selected harmonic constituents at the 9 tide-gauge stations (names indicated in bottom panels of each block). Colored symbols give the harmonic constants for the common period November 21, 2021 to May 22, 2022 according to the following color code that refers to data quality (see also legend): green (0–20% data gaps, good quality), yellow (20–40% gaps, medium quality), orange (40–60% gaps, poor quality). Black symbols correspond to the best six-month period in each station (see Appendix A3 for details). Vertical bars indicate the 95% confidence level. Blue lines and circles are the results for the model outputs, the blue shadow indicating the 95% confidence level. Numbers in x-axis in the panels of the top block are the amplitude difference (cm) between the model and best-six-month observations (blue circles - black circles) whereas they are phase difference, transformed to minutes of time, in the panels of the bottom block.

performance. The agreement between observed and modelled series is very good, with an average discrepancy less than 5 cm/s RMSE.

## 4. The tidal forcing scenarios

Next sections exploit the model outputs to investigate the response of the estuary to tidal forcing, according to the methodology and rationale explained here. With the aim of investigating the mutual interactions
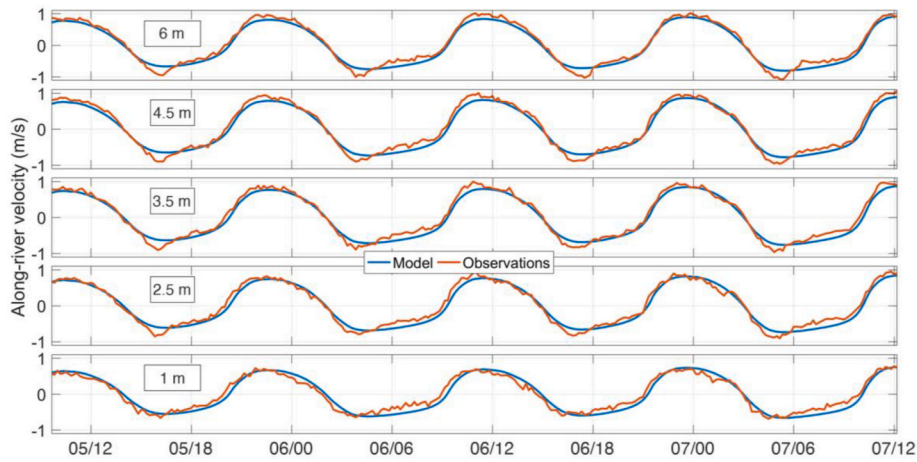
**Fig. 3.** Observed (orange) and modelled (blue) along-river velocity at five levels in a point located by the middle stretch of the estuary (red circle in Fig. 1c). Positive values correspond to landwards velocity. Numbers inside the rectangles is distance to the riverbed and x-axis indicate day/hour (dd/hh) of May 2021.

between constituents during low river freshwater discharges and on the non-linear behavior of the prevailing semidiurnal species (results presented in Section 5), several numerical experiments were conducted with a representative discharge of 25 m$^3$s$^{-1}$ (Bermúdez et al., 2021) for six months. The model was forced by a single tidal constituent (either, M$_2$ or S$_2$ or N$_2$) at the open boundary, and the results were compared with the outputs of the model forced by the entire set of constituents (control simulation). The resulting harmonic constants in these idealized experiments have been tagged with asterisks (M$_2$*, S$_2$*, N$_2$*). Given the proximity of the frequencies of these constituents, the experiments can be interpreted as if the estuary were forced with constituents of different amplitude (smaller, in this case) but the same frequency.

Fortnightly variations of the semidiurnal tide are investigated in more detail. To this aim, tides of varying intensity within the spring-neap tidal range were reconstructed using the four prevailing semi-diurnal constituents M$_2$, S$_2$, N$_2$ and K$_2$. Any of them can be expressed as:

$$\eta_j(x,t) = a_j(x)\,cos\,[\omega_j t - \varphi_j(x)] \qquad [4]$$

where $\eta_j(x,t)$ is the value of tidal constituent $j$ ($j$ = M$_2$,S$_2$,N$_2$,K$_2$) at time $t$ and location $x$, and $a_j(x)$ and $\varphi_j(x)$ are the harmonic constants (amplitude and phase, respectively). Spring tides happen when these constituents are in phase and neap tides when they are out of phase with respect to the reference M$_2$. The scheme in Table 1 considers several possible combinations that lead to different tidal strengths.

Let us consider the largest tide (equinoctial spring tide in Table 1) that occurs when the four constituents are in phase at the mouth ($x = x_0$). This condition must be met, as the tide in the estuary comes from

the ocean. The reconstructed tide, $\eta_r$, at a generic instant $t^*$ and location $x$ is:

$$\eta_r(x,t^*) = \sum_j a_j(x)\,cos\,[\omega_j t^* - (\varphi_j(x) - \varphi_j(x_0))] \qquad [5]$$

with term $(\varphi_j(x) - \varphi_j(x_0))$ ensuring the required in-phase condition of all constituents at the mouth (all of them having zero phase there). To allow for propagation, let us consider a short time interval around $t^*$ during which phase variation differences arising from $\omega_j t$ are negligible. This is equivalent to assuming that, during such a short interval, all constituents have the same frequency as the prevailing M$_2$ constituent. $\eta_r(x,t^*)$ can be expressed in the format of Equation [4] without loss of generality by defining $a_r(x)$ and $\varphi_r(x)$ as:

$$a_r(x) = \sqrt{\left(\sum_j a_j\,cos\,[\varphi_j'(x)]\right)^2 + \left(\sum_j a_j\,sin\,[\varphi_j'(x)]\right)^2} \qquad [6.a]$$

$$\varphi_r(x) = tan^{-1}\left[\frac{\sum_j a_j\,sin\,[\varphi_j'(x)]}{\sum_j a_j\,cos\,[\varphi_j'(x)]}\right] \qquad [6.b]$$

with $\varphi_j'(x) = \varphi_j(x) - \varphi_j(x_0)$. They are interpreted as pseudo-harmonic constants representing the spring tide and are presented in Table 1, including in the summation the constituents specified in the second column. To account for the phase opposition in neap tide cases, $\pi$ was added to $\varphi_j'(x)$.

**Table 1**
Reconstructed tidal strengths using the prevailing semidiurnal constituents, and some characteristics of the resulting tide. First column put names to the cases analyzed; second column indicates the constituents involved in each case and the corresponding amplitude in brackets, which are all in-phase at the mouth of the estuary for spring-tide cases and out-of-phase respect to M$_2$ for neap-tides. Third column is the phase difference between the head (end) and the mouth ($x_0$) of the estuary. Fourth and fifth columns indicate the mean celerity of the wave in the whole and in the uppermost 20 km of the estuary, respectively. Sixth column is the time taken by the wave to travel from the mouth up to Seville Port (km 77), which is not distance divided by column four because wave celerity is not constant. Seventh column is the amplification factors at Seville and at the estuary's head (Seville/head). Last column indicates the position of the point of minimum amplitude (dots in Fig. 5a).

| Case study | Constituents [amplitude (cm)] | $\varphi$ (head) -$\varphi$ ($x_0$) (degrees) | Phase-speed Whole estuary (ms$^{-1}$) | Phase-speed, Upper estuary (ms$^{-1}$) | Elapsed time (h) | Amplification factor (Seville/head) | Point of minimum amplitude (km) |
|---|---|---|---|---|---|---|---|
| Equinoctial spring tide | M$_2$+S$_2$+N$_2$+K$_2$ [161.18] | 137.1 | 6.814 | 9.169 | 4.067 | 0.938/1.091 | 36.2 |
| Spring tide | M$_2$+S$_2$+N$_2$ [151.54] | 136.5 | 6.841 | 9.257 | 4.056 | 0.950/1.105 | 35.8 |
| Weak spring tide | M$_2$+S$_2$ [131.79] | 136.4 | 6.847 | 9.275 | 4.052 | 0.956/1.111 | 35.8 |
| Reference | M$_2$ [97.49] | 133.9 | 6.976 | 9.670 | 3.998 | 1.016/1.182 | 33.8 |
| Weak neap tide | M$_2$-S$_2$ [63.19] | 129.7 | 7.200 | 10.487 | 3.908 | 1.134/1.324 | 31.2 |
| Neap tide | M$_2$-S$_2$-N$_2$ [43.44] | 127.0 | 7.353 | 10.997 | 3.847 | 1.247/1.459 | 29.0 |
| Equinoctial neap tide | M$_2$-S$_2$-N$_2$-K$_2$ [33.8] | 123.8 | 7.544 | 11.742 | 3.776 | 1.394/1.643 | 24.6 |

In order to investigate the estuary's response to the frequency of the forcing tides and its resonant behavior (Section 6), a series of experiments were conducted where a tide of a single harmonic with the amplitude of the current M$_2$ constituent and varying frequency (from 0.02 to 0.25 cph) was prescribed at the open boundary. This procedure is similar to the one used by Gao and Adcock (2017) in their study of the Bristol Channel resonance. To perform a sensitivity analysis of the forcing parameters, the experiment was repeated for the amplitudes of the case studies shown in Table 1, keeping the friction coefficient used in the calibrated model ($k_s = 1.5 \cdot 10^{-4}$ m). A second set of experiments was conducted modifying the coefficient $k_s$ from $1.5 \cdot 10^{-5}$ m to $1.5 \cdot 10^{-3}$ m to investigate the role of friction, maintaining the forcing amplitude constant and equal to that of M$_2$ (Table 1).

## 5. Interaction between semidiurnal constituents

### 5.1. Spatial patterns of semidiurnal constituents

Solid lines in Fig. 4a show the amplitudes of the three largest semidiurnal constituents M$_2$, S$_2$ and N$_2$. Fig. 4b (solid lines) displays the amplification factor $a(x)/a_M$ ($a_M$ is the amplitude in the mouth of the estuary), which is greater for M$_2$ than for S$_2$ or N$_2$ everywhere. It is greater than one for M$_2$ in the upper stretch of the estuary (landwards of $x = 75$ km approximately), reaching a value of 1.2 at the estuary's head. On the other hand, it is always less than one for S$_2$ with a maximum at the head of 0.9. N$_2$ lies in between (breaking the amplitude ranking of the three constituents) with values very slightly over one in the uppermost ten km of the estuary. Solid lines in Fig. 4c show the expected monotonous upstream increase of phases, with slightly larger slopes for S$_2$ and N$_2$ than for M$_2$. Consequently, the phase difference $(\varphi_{S2} - \varphi_{M2})$ is greater in the head than in the mouth of the estuary. This difference determines the delay interval of the spring tide with respect to the full/new moon, when the tidal driving forces are maximum. It is known as the *age of the tide* and is computed as $(\varphi_{S2} - \varphi_{M2})/(\omega_{S2} - \omega_{M2})$ and gives ages of $\sim 1.2$ days at the mouth and $\sim 1.8$ days at the head of the estuary from the phases in Fig. 4c. The first value at the mouth is obviously related to the open ocean tide, where the age of the tide is caused by friction in ocean basins with resonant frequencies close to the semidiurnal tidal frequencies (Garrett and Munk, 1971), whereas the landward increase is consequence of friction, in the same manner as it
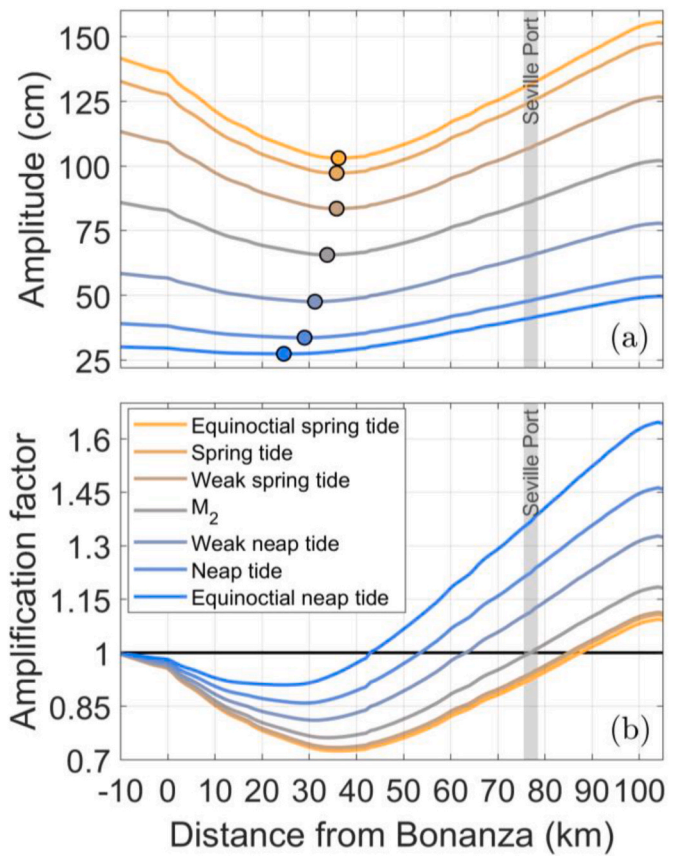


**Fig. 5.** Amplitude (a) and amplification factor (b) for the tidal scenarios described in Table 1. The position of the point of minimum amplitude for each case is indicated with dots of the same color code in panel a). Vertical grey line locates Seville Port in the estuary.

happens in large continental shelf areas of enhanced energy dissipation (Webb, 1973).

The S$_2$ phase retardation can be also addressed by estimating a local propagation speed $c(x) = \omega[\Delta x / \Delta\varphi]$, with $\Delta\varphi$ the phase difference
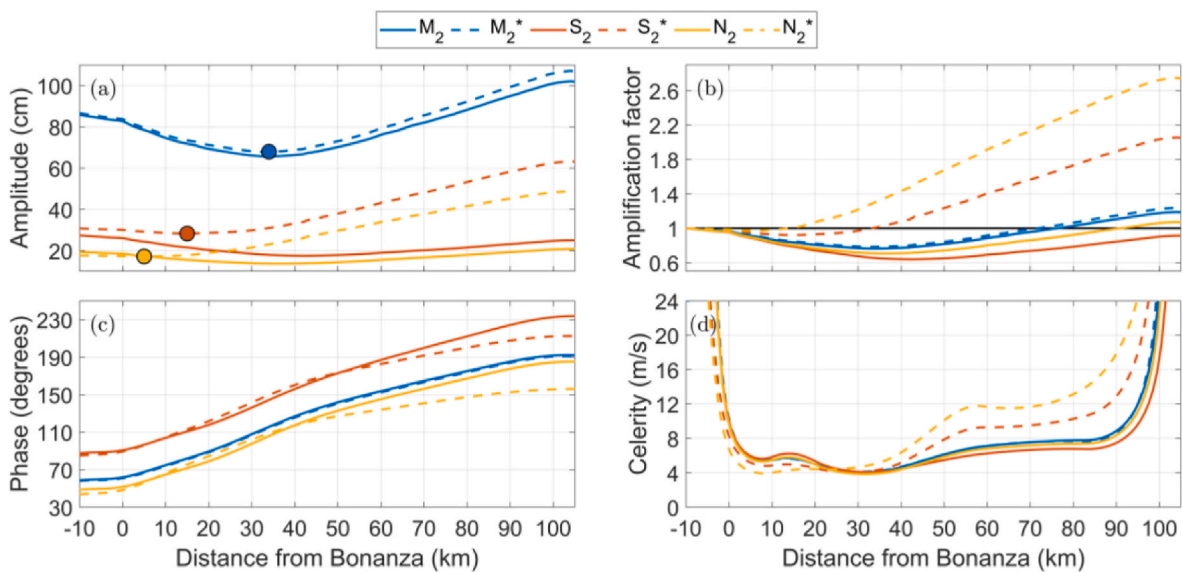


**Fig. 4.** Amplitude (a), amplification ratio (b), phase (c) and celerity (d) of the three principal constituents in the GE. The control case (solid lines) is the result of considering the joint effect of all constituents in the open boundary (control simulation), whilst the dashed lines refer to the constituents forced separately. The position of the point of minimum amplitude is indicated for the constituents forced separately with dots of the same color code.

between two points $\Delta x$ apart, and $\omega$ the frequency. Results are displayed by the solid lines in Fig. 4d (to prevent spikes, $\varphi(x)$ has been spatially smoothed prior to computing $c(x)$). Wave speed exhibits minimum values (4 ms⁻¹) around km 30–35, at the same place where amplitudes also do, and increase faster and faster as the head of the estuary is approached. As bathymetry becomes shallower in this region, the phase speed should decrease. However, in this upper stretch, the tide behaves like a quasi-standing wave due to wave reflection at the dam (Díez-Minguito et al., 2012b) and the increase in Fig. 4d is the expected result (phase speed is infinite for standing waves). With this exception near the head and in $x < 0$, outside the estuary, where water depth increases quickly, $c(x)$ is always smaller than the speed of frictionless long waves ($c = \sqrt{gH} \approx 8$ ms⁻¹ for a mean depth $H$ of 6.5–7 m) due to friction. The lower the $\Delta\varphi(x)$, the higher the $c(x)$, which results in M$_2$ having a slightly higher speed than S$_2$ and N$_2$ (Fig. 4d). The diminished speed of the last two could be attributed to increased friction, leading in turn to the increase of the time interval between spring tide and new/full moon.

### 5.2. Non-linear behaviors of semidiurnal constituents

Dashed lines in Fig. 4 presents the results of the idealized experiments with M$_2$*, S$_2$* and N$_2$* (see Section 4) using the same color code as the tidal forcing with all constituents. M$_2$* slightly increases its amplification factor to 1.23 at the estuary's head, the site of the greatest increase. Changes in phase and wave speed changes are even smaller. On the contrary, S$_2$* and N$_2$* show changes of the amplification factor over 250% compared to the control simulation (2.1 and 2.8, respectively, Fig. 4b). Wave speeds (Fig. 4d) also increase rapidly in the upper stretch of the estuary. Now, amplitude, amplification factor and wave speed follow the rank order of M$_2$, S$_2$ and N$_2$ in the equilibrium tide: the weaker the constituent, the greater the amplification and, expectedly, the wave speed.

The new patterns of the fictitious constituents reveal the importance of friction. The spatial pattern of the harmonic constants is the outcome of intricate relationships between tidal damping/amplification and wave celerity, which are influenced by channel convergence, bottom friction and the reflected wave in Alcalá del Río dam. Forcing the model with M$_2$* uniquely does not significantly modify the control situation as it dominates over all other constituents and determines the overall tidal pattern of the tide in the estuary. However, if only S$_2$* is at work, the results are notably different. Among the three processes at play, wave reflection, channel convergence and friction, the latter is the most affected by the tidal forcing reduction. As tidal current amplitude is roughly proportional to the tidal amplitude, the reduction of $\sim 2.5$ in amplitude (ratio M$_2$*/S$_2$*) implies a similar ratio in tidal currents and a quadratic friction ratio of $\sim 6.25$. Therefore, tidal damping due to friction is largely reduced, which explains the increased S$_2$* amplification factor (Fig. 4b). Friction-induced retardation of the phase speed would be also diminished and, hence, the increased wave celerity (see Fig. 4d). The same applies to N$_2$*, although the variations are even larger due to the smaller amplitude of the constituent.

### 5.3. Fortnightly variation of the semidiurnal tide: the spring-neap tidal cycle

When semidiurnal constituents are in phase (spring tide), friction and tidal damping along the estuary are enhanced. Although the tidal range throughout the estuary is greater than in the rest of the tidal scenarios (Fig. 5a), the amplification factor upstream is less due to the increased friction (Fig. 5b). In terms of harmonic constants, such pattern requires a reduction of the amplitude and the amplification factor with distance of the real S$_2$ when compared with its virtual counterpart S$_2$*, which is free from M$_2$ interaction (Fig. 3a and b). As a consequence, the clear "V-shape" exhibited by M$_2$ almost vanishes in the case of S$_2$, which

shows a more flattened pattern (Fig. 4a).

Fig. 5a shows the pseudo-amplitudes for the different tidal forcing experiments in Table 1. Trivially, they decrease from equinoctial spring to equinoctial neap. Pseudo-phase differences between the head and the mouth of the estuary also decrease with the tidal strength (column #3, Table 1), implying that larger tides propagate slower (column #4, Table 1) as a consequence of enhanced friction linked to stronger tidal currents. Tides take a shorter time to reach Seville Port from the mouth in neap than in spring tides, with differences of up to 18 min (column #6, Table 1). The amplification factor is significantly augmented in neap tides, when tidal currents and friction diminish (Fig. 5b). At very weak neap tides, its pattern recalls the one of the hypothetical S$_2$* in Fig. 4b (in fact, tidal amplitude in equinoctial neap is barely 10% greater than that of S$_2$* at the mouth).

All this leads to the fact that the region of the estuary where the tidal range is greater than at the mouth increases its size as the tidal strength diminishes (regions with amplification factor greater than one in Fig. 5b). In particular, the tidal range in spring tides is greater at the mouth than nearby Seville Port, but it is smaller in neap tides, a fact previously noted by Wang et al. (2014). A similar pattern is observed in the location of the virtual node (point of minimum amplitude, Fig. 5a) which moves towards the mouth of the estuary as the tidal strength decreases (see last column of Table 1). This result is consistent with the analytical study conducted by Cai et al. (2016) on resonance in semi-closed convergent tidal channels.

## 6. Frequency response in the GE: tidal resonance

According to Cai et al. (2016), the tidal amplitude or amplification factor at the resonant frequency reaches its maximum value at the reflecting wall in the head of the estuary. Within this approach and using analytical methods these authors estimated in 35 h the resonant period of the GE. Fig. 6 displays contours of the amplification factor as a function of frequency and distance from the mouth for different tidal scenarios. For average tides (the case of M$_2$ forcing, Fig. 6c), maximum amplification at the reflecting wall occurs around the frequency band of species #1 ($\omega \sim 0.04$ cph, $T \sim 25$ h). This suggests a period of resonance somewhat less than the value provided by Cai et al. (2016). When the amplitude of the forcing decreases during neap tides (Fig. 6a and b), the maximum amplification shifts to higher frequencies and increases in magnitude, in agreement with Fig. 5, although it does not reach the semidiurnal band. Conversely, during spring tides (Fig. 6d and e) the maximum shifts toward lower frequencies.

Black dashed lines show how the location of the point of minimum amplitude or virtual node (Cai et al., 2016) moves towards the mouth as frequency decreases. For frequencies smaller than $\omega \sim 0.04$ cph, the point no longer exists, indicating that tidal amplitude increases monotonically from the mouth upstream. Phases increase rather linearly for high frequencies (Fig. 6f to j) and isolines bend to flatten towards the upper stretch of the estuary as frequency decreases. This pattern is relatively insensitive to the strength of the tidal forcing at the mouth. The flattening of isolines in the low frequency range increases the spatially-averaged wave celerity in the estuary, as shown by the celerity profiles in Fig. 6k to o. They remain around 7 ms⁻¹ for most of the explored frequency interval and increases quickly for diurnal and lower frequencies. As expected, it approaches asymptotically infinity as frequency tends to zero. Since the slope of phase isolines is inversely proportional to celerity, wave speed near the mouth is lower than in the upper stretch of the estuary (Fig. 6f to o), agreeing with the results discussed in Section 4 on semidiurnal constituents. Within this stretch, celerity increases noticeably for frequencies near and below the resonance frequency, as it can be deduced from the flattened isohalines beyond $x = 20$ km.
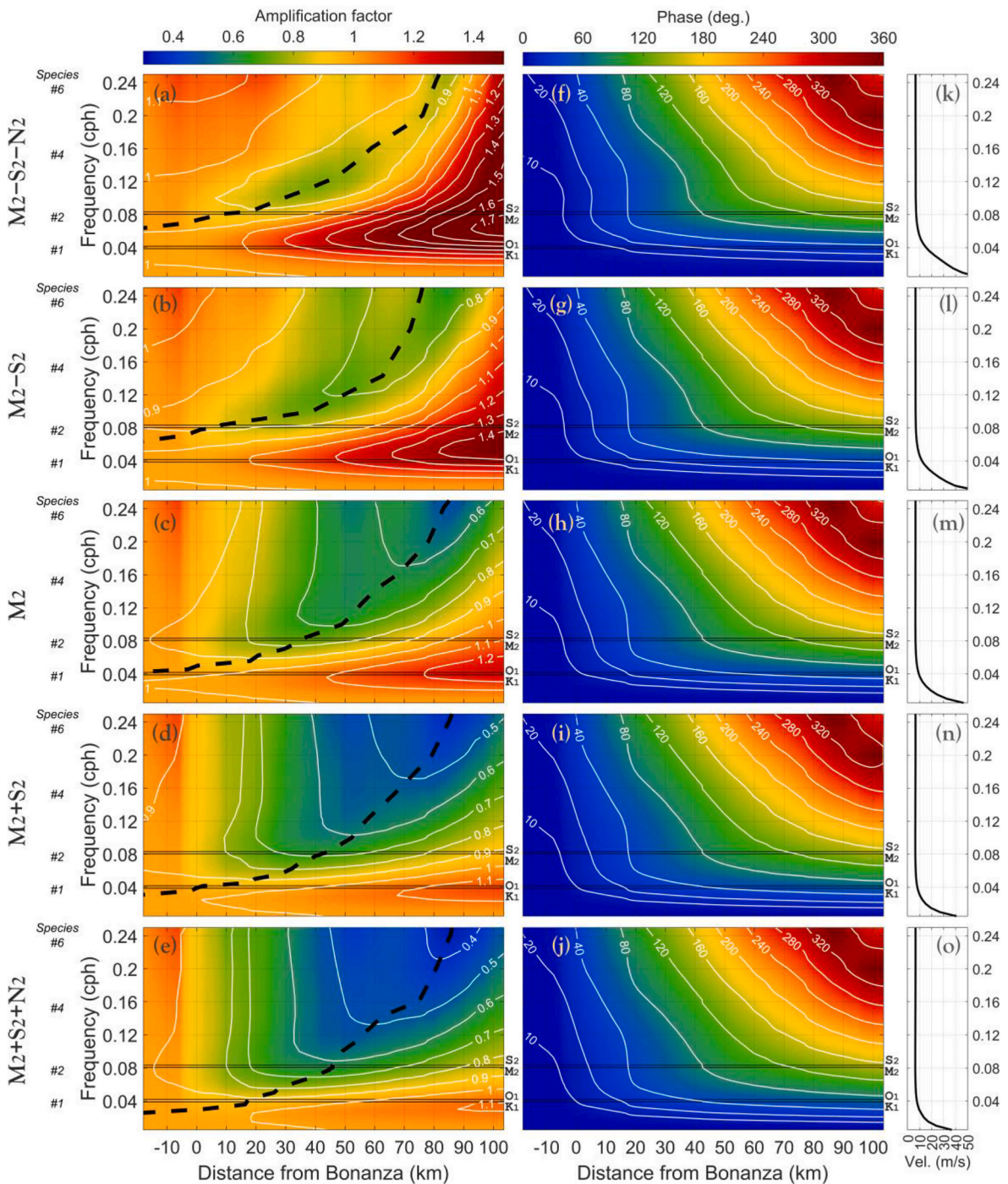
**Fig. 6.** Left column: Contours of amplification factor as a function of distance and frequency for tidal forcing at the mouth corresponding to amplitudes of M₂−S₂−N₂ and M₂−S₂ (panels a,b; neap tide situation), M₂ (panel c; average tide) and M₂+S₂ and M₂+S₂+N₂ (panels d,e; spring tide situation). Thick dashed black lines indicate the frequency-dependent location of the amplitude minimum. Tidal species are shown on the left of the y-axis and constituents S₂, M₂, K₁ and O₁ have been depicted as horizontal black lines. Center column (panels f to j): Contours of phase for the same range of tidal forcing as in the left column. They are referred to the value of zero prescribed at the mouth. Right column (panels k to o): Spatially averaged phase speed computed from phases in the center column.

### 6.1. The role of friction in the frequency response and resonance in the GE

Fig. 7a shows that the amplification factor increases as friction decreases, as expected in dissipative systems. The increase is more noticeable for higher frequencies, while all curves converge to one when frequency approaches zero. As friction increases, the resonant peak decreases and shifts towards lower frequencies. For very low friction ($k_s = 1.5 \cdot 10^{-5}$ m), the peak occurs at $\omega = 0.0528$ cph ($T = 18.9$ h). It occurs at $\omega = 0.0454$ cph ($T = 22.0$ h) for the reference case ($k_s = 1.5 \cdot 10^{-4}$ m),

and at $\omega = 0.0356$ cph ($T = 28.1$ h) for strong friction ($k_s = 1.5 \cdot 10^{-3}$ m). In all cases, the resonant period is significantly smaller than $T = 35$ h suggested in Cai et al. (2016) in their analytical study. Resonance will continue to occur at diurnal frequencies, regardless of any variations of the friction coefficient.

A similar analysis was conducted by maintaining the coefficient $k_s$ constant ($k_s = 1.5 \cdot 10^{-4}$ m) and varying the amplitude of the tidal forcing (Fig. 7b). As quadratic friction is proportional to the amplitude of the tide via tidal currents, augmenting the amplitude increases
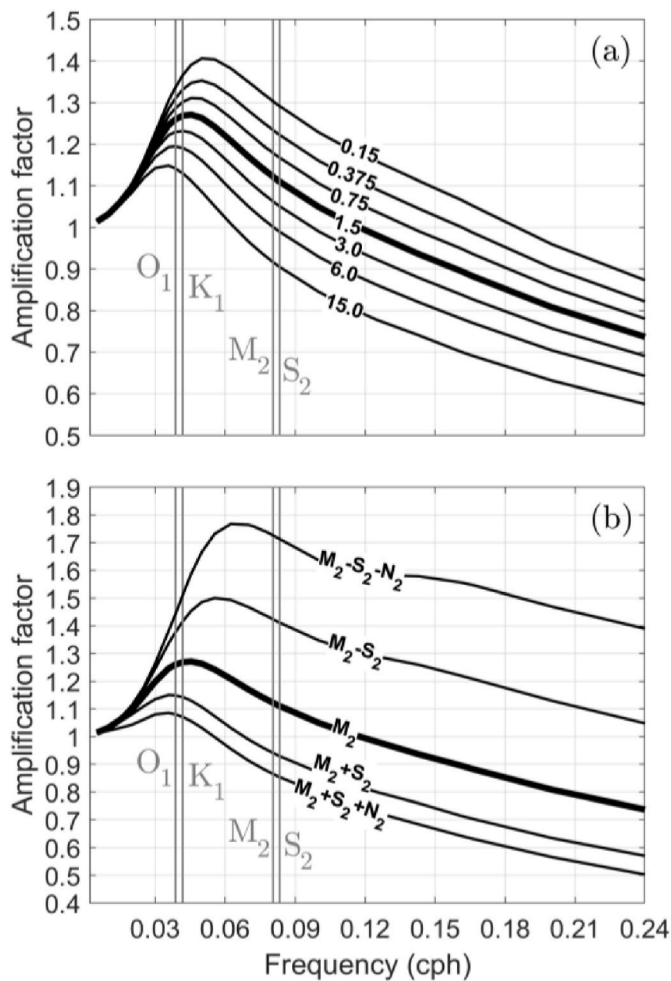
**Fig. 7.** *(a) Amplification factor at the head of the estuary in Alcalá del Río dam as a function of the frequency for different coefficients $k_s$ ($10^{-4}$ times the numbers in the labels). Thick line corresponds to the value used in the calibrated model ($k_s = 1.5 \cdot 10^{-4}$ m). Frequencies of semidiurnal $M_2$ and $S_2$, and diurnal $K_1$ and $O_1$ constituents are indicated. (b) Amplification factor for a fixed coefficient $k_s = 1.5 \cdot 10^{-4}$ m and various amplitudes of the tidal forcing, as indicated in the legend.*

friction, resulting in similar outcomes to those obtained by increasing the coefficient. The resonant peak is situated around $K_1$ and $O_1$ frequencies in spring tides, although its magnitude is significantly reduced due to the intense friction.

## 7. Discussion

A three-dimensional numerical model, based on Delft3D code (Deltares, 2022), has been implemented in the GE, a mesotidal estuary whose hydrodynamics is basically determined by the tide at the mouth. For this reason, model calibration compares the harmonic constants derived from the numerical outputs and from a network of tide gauges operating along the estuary. Both sets of constants agree quite satisfactorily, especially for the prevailing semidiurnal constituents (Fig. 2). The model is then used to investigate aspects of the GE dynamics under low river freshwater discharges.

The amplitude of the main $M_2$ constituent displays a V-shape with minimum amplitude around 35 km upstream the mouth of the estuary as a result of physical processes that include channel convergence, friction and reflection at the dam in the head (Díez-Minguito et al., 2012a, 2012b). The V-shape of $S_2$ and $N_2$ is much less pronounced due to their diminished amplitude at the estuary's head, as shown by the amplification factor (ratio of amplitudes relative to the amplitude at the mouth,

Fig. 4b). This is a consequence of their interaction with $M_2$ because of the role of quadratic friction on the propagation of the tide. Cai et al. (2018) obtained similar results using an analytical model that employed Chebyshev polynomials to quantify the effective friction experienced by the different semidiurnal constituents. Numerical experiments were conducted to simulate tides in the estuary, forced by a unique virtual constituent with the same amplitude as the real one at the mouth. The results showed no significant differences for $M_2$, but important differences for $S_2$ and $N_2$ (Fig. 4). The amplification factor of virtual constituents $S_2^*$ and $N_2^*$ at the head greatly exceed that of $M_2$ (or $M_2^*$, Fig. 4b), suggesting a reduced role of friction in favor of wave reflection in the dam. This reflection is responsible for the formation of a standing-wave-like pattern (Díez-Minguito et al., 2012a), a fact confirmed by the flattening of $S_2^*$ and $N_2^*$ phases and the significant increase of their wave celerity near the head (Fig. 4c and d).

The response of the estuary to tides of different realistic tidal amplitudes was analyzed in a set of experiments that superimposed the four largest semidiurnal constituents to produce a range of tidal strength from very neap to very spring tides (Table 1). Channel convergence, friction and the effect of tidal reflection at the dam are the three fundamental processes that determine the tidal pattern in the estuary (Díez-Minguito et al., 2012a; Cai et al., 2016). The first one remains unchanged in the experiments. Therefore, the changing response depends on the other two, of which quadratic friction is the most influential one. Large tidal ranges increase friction and reduce the upstream amplitude, whereas the diminished friction in neap tides enhances the amplification factor at the head (Fig. 5b). The damping effect of friction would also affect the formation of the standing-wave-like pattern caused by the wave reflection. Weaker friction allows for greater amplitudes at the reflecting wall and larger reflected energy, which in turn increases the extension of the standing-wave-like region. The seawards displacement of the amplitude minimum when tidal strength (and, hence, friction) diminishes suggests such enlargement (Fig. 5a). The rise of wave celerity near the reflecting wall also points at an enhanced standing-wave-like pattern, as discussed in Section 5 (Fig. 4d). Column #5 of Table 1 shows that this celerity in neap tides increases by $\sim$ 28% compared with spring tides. In contrast, the spatially-averaged celerity in the entire estuary (column #4, Table 1) only increases by $\sim$ 10%, which suggests the growing importance of the standing-wave-like region (i.e., the wave reflection) on the response of the estuary as tidal forcing decreases. Or, contrary, the decreasing importance of wave reflection in spring tides when friction is at its maximum.

Resonance in the estuary was investigated by examining the response of the amplification factor at the reflecting wall. For average tides (represented by $M_2$ forcing alone), maximum response occurs at diurnal frequencies and shifts to higher (lower) frequencies in neap (spring) tides (Fig. 6a–e). In all cases the corresponding period is consistently less than the resonant period of 35 h postulated by Cai et al. (2016). For a given amplitude, tidal velocity, and hence, quadratic friction and dissipation increase with frequency, which favors the progression of the virtual node or point of minimum amplitude upstream (Fig. 6a–e), in agreement with Cai et al. (2016). The contrary happens for decreasing frequencies that displace the virtual node towards the mouth of the estuary until it eventually disappears for frequencies close to the resonance in the diurnal band.

The study has been extended to different values of the friction coefficient (Fig. 7a). An unrealistic coefficient $k_s = 1.5 \cdot 10^{-3}$ m, one order of magnitude greater than the value of the calibrated model, causes the resonance peak to move to $\omega = 0.0356$ cph or a period $T = 28.1$ h (Fig. 7a), a value noticeably smaller than the one in the analytical study of Cai et al. (2016). Differences likely arise from the necessary simplifications of the analytical approach used by these authors and could be associated with non-linearity. Notice that variations of the forcing amplitude lead to similar results (Fig. 7b), since the quadratic friction is proportional to the tidal amplitude via tidal currents.

The results of this study are based on the accuracy of the numerical

model, which has already been discussed. A limitation to this accuracy arises from the use of fresh water to irrigate large areas of rice fields. Great volumes of water are removed and subsequently returned in a smaller fraction to the estuary. The way and specific locations where these processes occur are not well documented and therefore cannot be suitably prescribed in the model boundary conditions. The rice fields are located towards the middle of the estuary (Isla Mínima, see Fig. 1b and Google image in Fig. 1c), which is the area where the comparison of harmonic constants indicates minor discrepancies (Fig. 2). Despite these minor discrepancies, the overall good performance of the numerical model supports the results presented here.

## 8. Conclusions

The implemented 3D numerical model satisfactorily reproduces the dynamics of the estuary. Its tidally-driven nature makes the harmonic analysis applied to observations and model outputs be the best tool for validation purposes. On average, the amplitudes of the dominant semidiurnal constituents differ by less than 4% and the phases by less than $6°$ ($\sim$5 min for semidiurnal frequencies), values that diminish if tide-gauge stations of dubious data quality in the middle of the estuary are excluded from the comparison. On the other hand, the RMSEs of observed and modelled water levels at Bonanza (near the mouth) and Seville ($\sim$80 km upstream) are 1.3 cm and 1.1 cm, respectively (Pearson correlation coefficients of 0.981 and 0.985). A similar comparison with a short time series of velocity profiles gives RMSEs of less than 5 cm/s.

The spatial pattern of tidal range in the estuary is rather sensitive to the spring-neap tidal cycle, a fact explained by the V-shaped spatial pattern of tidal amplitudes, which the model correctly reproduces. The V-shape is more conspicuous for $M_2$ than for $S_2$ and $N_2$ as a result of the interaction among constituents via friction. The consequence is a notable dependence of the amplification factor on the tidal amplitude (i. e., the spring-neap tidal cycle, see Fig. 5b). For instance, near Seville, far upstream in the estuary, the tidal range during spring tides is $\sim$95% of the range at the mouth (amplification factor $\sim$0.95), whereas it is $\sim$140% during weak neap tides (amplification factor $\sim$1.4). Furthermore, the weaker the tide, the closer to the mouth is the point of minimum tidal range and the larger the upstream extension where the amplification factor is greater than one. These features reveal the increasing effect of tidal reflection at the headwater dam, to the detriment of friction in the estuary, as tides weaken.

An analysis of the amplification factor at the head of the estuary for virtual forcing tides of the same amplitude and changing frequency was conducted to investigate resonance. For a forcing tide of $M_2$ amplitude, representative of average tides, the maximum amplification is found for

frequencies around 1 cpd ($\sim$25 h). Increasing the forcing amplitude shifts the maximum towards lower frequencies, while diminishing the forcing amplitude has the opposite effect. In all cases, the maximum occurs at a frequency distinguishably smaller than the resonance frequency given in previous studies (Cai et al., 2016). Larger friction coefficients for the same forcing amplitude displace the resonance to lower frequencies. Thus, increasing friction, either by changing the friction coefficient or the forcing amplitude, reduces the value of the resonance peak and shifts it to lower frequencies, in a manner that recalls the response of a linear forced oscillator to friction.

## CRediT authorship contribution statement

**P. Muñoz-Lopez:** Writing – review & editing, Writing – original draft, Visualization, Validation, Software, Methodology, Investigation, Formal analysis, Data curation. **I. Nadal:** Writing – review & editing, Writing – original draft, Visualization, Validation, Software, Methodology, Investigation, Formal analysis, Data curation. **J. García-Lafuente:** Writing – review & editing, Writing – original draft, Supervision, Project administration, Methodology, Investigation, Funding acquisition, Formal analysis, Data curation, Conceptualization. **S. Sammartino:** Writing – review & editing, Validation, Software, Resources, Data curation. **A. Bejarano:** Resources, Project administration, Funding acquisition.

## Declaration of competing interest

The authors declare the following financial interests/personal relationships which may be considered as potential competing interests:

Pablo Muñoz Lopez reports financial support was provided by Port Authority of Seville.

## Acknowledgements

## APPENDIX

### A1. Model grid implementation

The domain of the model extends from $5°\ 58'$ W to $6°\ 34'$ W and from $36°\ 39'$ N to $37°\ 31'$ N (Fig. 1b) and it is discretized by a curvilinear orthogonal grid of non-uniform resolution that follows the staggered Arakawa-C grid scheme. The domain comprises the primary tributaries of Brazo de la Torre and Gergal on the western margin of the estuary, the Guadaira river on the eastern margin, and the lateral extensions of Isleta (a disused abandoned meander) and Ante-Esclusa (the access gateway to Seville Port) on the eastern margin. The grid is bordered by a row of cells that protrude outward from the estuary to ensure effective capture of cell drying (refer to Fig. 1c).

The resolution along the longitudinal axis in the main channel varies horizontally from 328 m near the mouth to 6.2 m in some areas of the tributaries, with a mean value of 97 m. In the cross-river direction, the resolution varies from 127 m near the mouth to 6 m in the tributaries, with a mean value of 44 m. The maximum width of the estuary is 870 m within the estuary and 2.7 km near the mouth. The model uses a vertical sigma-coordinate system that comprises ten levels with thicknesses from top to bottom of, 2, 3, 4.5, 7, 16, 25.5, 18, 12, 8 and 4% of the local depth, respectively.

The grid outlines were defined by adapting splines to georeferenced orthophotos of the estuary using the free software QGIS. The RGFGRID tool, included in the Delft3D software (Deltares, 2018), was used to generate and orthogonalize the grid. Its resolution at meanders and tributaries junctions with the main channel was enhanced to achieve smooth transitions and the connecting cells were also carefully adjusted to ensure good orthogonality. The final grid, consisting of 924 x 372 cells, was divided into twelve sub-domains (the largest one of 148 x 14 cells) using the domain decomposition

tool of Delft3D, aimed at parallelizing the model and reducing the computation time. For a one-year simulation, parallelization reduces the time required from tens of days to 2.5 days with a time step of 0.3 min.

Bathymetry data were obtained from three different sources: i) Navigation channel depth from the estuary mouth to Seville collected in October 2021 by the Port Authority of Seville, ii) Data collected in year 2019 by the Seville Port Authority in the non-navigable portion of the estuary (Seville area to the estuary head in Alcalá del Río dam, Fig. 1b), the three tributaries of Brazo de la Torre, Guadaira, and Gergal as well as the Isleta extension, and iii) Bathymetry of all the estuary with special emphasis on the mouth-continental shelf area carried out by the Spanish Marine Hydrographic Institute in year 2017.

The depth of each cell was defined using one of two methods, depending on the number of available bathymetric data within it. If there were four or more data points available within the cell, the depth was assigned as the averaged value. Otherwise a triangular interpolation was applied. After the bathymetry was interpolated into the grid, the shores were reviewed and checked to ensure that the interpolation did not produce any spurious cells and that the water-land interface was accurately represented. The comparison of interpolated values with their position in the georeferenced orthophoto was used to carry out the checking. To assess all the tributaries and the area downstream from the Alcalá del Río dam, additional points were manually interpolated from the existing bathymetric data to facilitate water flow. Finally, a fixed value of 2 m above the mean waterlevel was assigned to the cells added in the river banks.

The water level is computed by the model at the cell centers, based on the maximum of the water level from the four nearest nodes of each cell, while velocity components are given perpendicular to the cell faces at their centers, following the geometry of the staggered Arakawa-C scheme. Depth is calculated as the mean of the water depths at the corners of each cell. Drying and flooding are checked using the center and faces of the cells.

*A2. Constituents*

Harmonic constants, along with their standard errors, have been specified at the estuary mouth as boundary conditions. These values were adapted from García-Lafuente (1986). Only major constituents were slightly tuned during the calibration process, which is physically supported by the fact that the harmonic constants correspond to the tide gauge station closest to the estuary mouth, which is Cádiz (see Fig. 1a), located some tens of kilometers away.

**Table A2**
Harmonic constants (amplitude, $a_I$, and phase, $\varphi_I$, and standard errors) of the constituents prescribed at the mouth of the estuary as boundary condition (from García-Lafuente, 1986). Harmonic constants of the major constituents that have been slightly tuned (amplitude, $a_C$, and phase, $\varphi_C$) during the calibration process along with the calibration correction (an additive term, in brackets) are highlighted in bold. This tuning is physically supported by the fact that the harmonic constants correspond to the tide gauge station closest to the estuary mouth, which is Cádiz (see Fig. 1a), located some tens of km away.

| Harmonic constituents | $a_I$ [cm] | $\varphi_I$ [°] | $a_C$ [cm] ($\Delta a$ [cm]) | $\varphi_C$ [°] ($\Delta \varphi$ [°]) |
|---|---|---|---|---|
| **$M_2$** | **106.79 ± 0.26** | **55.5 ± 0.5** | **97.49 (-9.30)** | **49.5 (-6)** |
| **$S_2$** | **37.82 ± 0.25** | **81.5 ± 0.5** | **34.30 (-3.52)** | **77.5 (-4)** |
| **$N_2$** | **22.80 ± 0.25** | **41.0 ± 1.0** | **19.75 (-3.05)** | **35 (-6)** |
| **$K_2$** | **11.14 ± 0.26** | **74.5 ± 1.5** | **9.64 (-1.50)** | **70 (-4.5)** |
| **$O_1$** | **7.13 ± 0.25** | **300.0 ± 2.0** | **-** | **313 (+13)** |
| **$K_1$** | **6.93 ± 0.25** | **42.0 ± 2.0** | **5.96 (-0.97)** | **50 (+8)** |
| SSA | 5.96 ± 0.25 | 68.0 ± 3.0 | – | – |
| $MU_2$ | 4.54 ± 0.26 | 22.0 ± 4.0 | – | – |
| $NU_2$ | 4.53 ± 0.25 | 32.0 ± 4.0 | – | – |
| $L_2$ | 4.53 ± 0.25 | 56.0 ± 6.0 | – | – |
| $P_1$ | 2.55 ± 0.25 | 34.0 ± 6.0 | – | – |
| $2N_2$ | 2.42 ± 0.25 | 24.0 ± 6.0 | – | – |
| MM | 2.05 ± 0.26 | 270.0 ± 7.0 | – | – |
| MF | 1.79 ± 0.25 | 133.0 ± 8.0 | – | – |
| $Q_1$ | 1.62 ± 0.26 | 258.0 ± 9.0 | – | – |
| $MNS_2$ | 0.83 ± 0.26 | 11.0 ± 18.0 | – | – |
| $LAM_2$ | 0.83 ± 0.26 | 147.0 ± 18.0 | – | – |
| $NO_1$ | 0.78 ± 0.25 | 323.0 ± 18.0 | – | – |
| MSF | 0.67 ± 0.25 | 1.0 ± 21.0 | – | – |
| $ETA_2$ | 0.51 ± 0.26 | 138.0 ± 27.0 | – | – |
| $OQ_2$ | 0.37 ± 0.25 | 12.0 ± 35.0 | – | – |
| $2Q_1$ | 0.37 ± 0.26 | 201.0 ± 36.0 | – | – |
| $MO_3$ | 0.32 ± 0.26 | 214.0 ± 40.0 | – | – |
| $RO_1$ | 0.32 ± 0.26 | 276.0 ± 41.0 | – | – |
| $J_1$ | 0.30 ± 0.25 | 86.0 ± 41.0 | – | – |
| $TAU_1$ | 0.29 ± 0.26 | 176.0 ± 47.0 | – | – |
| $SIG_1$ | 0.28 ± 0.25 | 241.0 ± 51.0 | – | – |

*A3. Water level and velocity data for model validation*

Water level data from nine tide gauges which provide good coverage of the GE, have been used. The Puertos del Estado (PDE) REDMAR network holds the longest records, with four radar tidal stations located along the navigable part of the estuary (yellow crosses in Fig. 1b). They are freely available at https://portus.puertos.es. The oldest station, Bonanza, has been recording water level every minute since 1992. Seville station, second-longest record, has been operative since 2010 with the same sampling rate. In spring of 2021, two new Miros Radar Sensors were installed in the middle stretch of the estuary at Puntal and Caseta (Fig. 1b), sampling every 5 min. All of them are Miros Radar Sensors. Water level series were also collected by the Confederación Hidrográfica del Guadalquivir (CHG) in the middle and upper estuary and the data are also freely available at https://www.chguadalquivir.es/saih/. The longest CHG records, with hourly sampling rates, are from Alcalá del Río dam, Isla Cartuja and Isla Mínima,

which have been operating since 1999. CHG recently installed two additional gauges in Vetalapalma and Queipo (Fig. 1b).
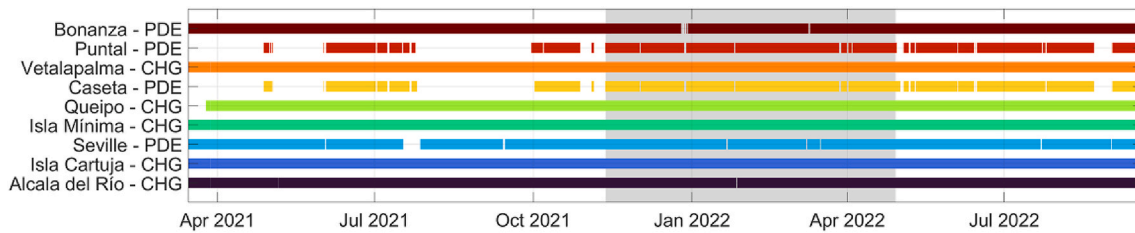


**Fig. A1.** Time coverage of tide gauge observations between January 2021 and October 2022. Names of the stations and responsible institutions are indicated on the left. Shaded rectangle refers to the six-month period used for the bulk of the validation. Names of the tide gauge stations, locations, time period and operating institutions are indicated.

A brief field experiment was conducted between the 5th and 7th of May 2021 to acquire velocity profiles using an Acoustic Doppler Current Profile (ADCP, Nortek AWAC 600 kHz) deployed in the middle of the estuary in the vicinity of Queipo station (see red dot in Fig. 1). The instrument was configured to provide the three velocity components every 10 min with vertical resolution of 50 cm in a mean water depth (referred to the mean surface level) of 8 m. Each profile was the result of averaging 540 s of sampling at a frequency of 2 Hz, corresponding to 1080 pulses. Along-river modelled velocity was interpolated in the vertical to correct for the effect of sigma coordinates and to match the levels of the ADCP.

The core of the model bathymetry was acquired in October 2021, a fact that must be considered for model validation as model outputs depend on the bathymetry. Only water level series after that date should be used for validation. Five out of the nine tidal stations start well before that date, while the remaining four started at the beginning of year 2021 (figure A1). The period November 2021–May 2022, long enough to resolve the main semidiurnal constituents, fulfils the condition and was initially used. However, data from certain stations within this window have questionable quality due to fragmented series, missing values caused by insufficient water depth, tide-gauge failures, and others factors such an unusual weather event that left the instrument out of service. As a result, the derived harmonic constants may also be of questionable quality (refer to the color code assigned to the harmonic constants in Fig. 2). To tackle this issue, harmonic constants using the six-month period of highest data quality for each station between January 2021, and October 2022, were computed and then compared with those produced by the model during the period of November 2021 to May 2022. The procedure is justified because harmonic constants computed during different periods must keep their values if no significant bathymetric changes occur in between.

# References

Álvarez, O., Tejedor, B., Vidal, J., 2001. La dinámica de marea en el estuario del Guadalquivir: un caso peculiar de «resonancia antrópica». Física Tierra 13, 11–24. ISSN: 0214-4557. https://dialnet.unirioja.es/servlet/articulo?codigo=268752.

Bermúdez, M., Vilas, C., Quintana, R., González-Fernández, D., Cózar, A., Díez-Minguito, M., 2021. Unraveling spatio-temporal patterns of suspended microplastic concentration in the Natura 2000 Guadalquivir estuary (SW Spain): observations and model simulations. Mar. Pollut. Bull. 170, 112622 https://doi.org/10.1016/j.marpolbul.2021.112622.

Cai, H., Toffolon, M., Savenije, H.H.G., 2016. An analytical approach to determining resonance in semi-closed convergent tidal channels. Coast Eng. J. 58 (3) https://doi.org/10.1142/S0578563416500091, 1650009-1-1650009-37.

Cai, H., Toffolon, M., Savenije, H.H.G., Yang, Q., Garel, E., 2018. Frictional interactions between tidal constituents in tide-dominated estuaries. Ocean Sci. 14 (4), 769–782. https://doi.org/10.5194/os-14-769-2018.

Deltares, 2018. RGFGRID. Generation and manipulation of structured and unstructured grids, suitable for Delft3D-FLOW, Delft3D-WAVE or D-flow Flexible mesh. User manual. Released for: Delft3D FM suite 2018 & D-HYDRO suite 2018. Version: 5.00 SVN revision: 57594. August 30, 2018. In: Published by Deltares, Boussinesqweg 1, 2629 HV Delft, P.O. 177, 2600 MH Delft, The Netherlands.

Deltares, 2022. Delft3D-FLOW. Simulation of multi-dimensional hydrodynamic flows and transport phenomena, including sediments. User Manual. Hydro-Morphodynamics. Version: 3.15 SVN revision: 57696 August 30, 2018. In: Published and Printed by Deltares, Boussinesqweg 1, 2629 HV Delft, P.O. 177, 2600 MH Delft, The Netherlands.

Dias, J.M., Valentin, J.M., Catarina, M., 2013. A numerical study of local variations in tidal regime of Tagus estuary, Portugal. PLoS One. https://doi.org/10.1371/journal.pone.0080450.

Díez-Minguito, M., Baquerizo, A., Ortega-Sánchez, M., Navarro, G., Losada, M.Á., 2012a. Tide transformation in the Guadalquivir estuary (SW Spain) and process-based zonation. J. Geophys. Res. 117, C03019 https://doi.org/10.1029/2011JC007344.

Díez-Minguito, M., Baquerizo, A., Ortega-Sánchez, M., Ruiz, I., Losada, M.Á., 2012b. Tidal wave reflection from the closure dam in the Guadalquivir estuary (SW Spain). Coastal Engineering Proceedings 1. https://doi.org/10.9753/icce.v33.currents.58.

Donázar-Aramendía, I., Sánchez-Moyano, J.E., García-Asencio, I., Miró, J.M., Megina, C., García-Gómez, J.C., 2018. Maintenance dredging impacts on a highly stressed estuary (Guadalquivir estuary): a BACI approach through oligohaline and polyhaline habitats. Mar. Environ. Res. 140, 455–467. https://doi.org/10.1016/j.marenvres.2018.07.012, 0141-1136.

Forester, C.K., 1977. Higher order monotonic convective difference schemes. J. Comput. Phys. 23 (1), 1–22. https://doi.org/10.1016/0021-9991(77)90084-5.

Gao, C., Adcock, T.A.A., 2017. On the tidal resonance of the Bristol Channel. Int. J. Offshore Polar Eng. 27 (2), 1. https://doi.org/10.17736/ijope.2017.as19.

Garel, E., Cai, H., 2018. Effects of tidal-forcing variations on tidal properties along a narrow convergent estuary. Estuar. Coast 41 (7), 1924–1942. http://www.jstor.org/stable/44858200.

García-Lafuente, J.M., 1986. Variabilidad del nivel del mar en el Estrecho de Gibraltar: Mareas y oscilaciones residuales. PhD. University of Malaga.

García-Lafuente, J., Delgado, J., Navarro, G., Calero, C., Díez-Minguito, M., Ruiz, J., Sánchez-Garrido, J.C., 2012. About the tidal oscillations of temperature in a tidally driven estuary: the case of the Guadalquivir estuary, southwest Spain. Estuar. Coast Shelf Sci. 111, 60–66. https://doi.org/10.1016/j.ecss.2012.06.007.

Garrett, C., Munk, H.W., 1971. The age of the tide and the "Q" of the oceans. Deep Sea Research and Oceanographic Abstracts 18 (5), 493–503. https://doi.org/10.1016/0011-7471(71)90073-8.

Gomiz-Pascual, J.J., Bolado-Penagos, M., Gonzalez, C.J., Vazquez, A., Buonocore, C., Romero-Cozar, J., Perez-Cayeiro, M.L., Izquierdo, A., Alvarez, O., Mañanes, R., Bruno, M., 2021. The fate of Guadalquivir River discharges in the coastal strip of the Gulf of Cadiz. A study based on the linking of watershed catchment and hydrodynamic models. Sci. Total Environ. 795 https://doi.org/10.1016/J.SCITOTENV.2021.148740.

Lesser, G.R., Roelvink, J.A., van Kester, J.A.T.M., Stelling, G.S., 2004. Development and validation of a three-dimensional morphological model. Coastal Engineering 51, 883–915. https://doi.org/10.1016/j.coastaleng.2004.07.014.

Pawlowicz, R., Beardsley, B., Lentz, S., 2002. Classical tidal harmonic analysis including error estimates in MATLAB using T_TIDE. Comput. Geosci. 28 (8), 929–937. https://doi.org/10.1016/S0098-3004(02)00013-4. ISSN 0098-3004.

Ruiz, J., Polo, M.J., Díez-Minguito, M., Navarro, G., Morris, E., Huertas, E., Caballero, I., Contreras, E., Losada, M., 2015. The Guadalquivir estuary: a hot spot for environmental and human conflicts. Environmental Management and Governance Coastal Research Library 8, 199–232. https://doi.org/10.1007/978-3-319-06305-8_8.

Siles-Ajamil, R., Díez-Minguito, M., Losada, M.Á., 2019. Tide propagation and salinity distribution response to changes in water depth and channel network in the Guadalquivir River Estuary: an exploratory model approach. Ocean Coast Manag. 174, 92–107. https://doi.org/10.1016/j.ocecoaman.2019.03.015. ISSN 0964-5691.

Stelling, G.S., Lendertse, J.J., 1991. Approximation of convective processes by cyclic ACI methods. In: Spaulding, M.L., Bedford, K., Blumberg, A. (Eds.), Estuarine and Coastal Modeling, Proceedings 2nd Conference on Estuarine and Coastal Modelling, vol. 90. Tampa, ASCE, pp. 771–782, 280, 286, 291. https://cedb.asce.org/CEDBsearch/record.jsp?dockey=0123745.

Uittenbogaard, R.E., Van Kester, J.A.T.M., Stelling, G.S., 1992. Implementation of three turbulence models in 3D-TRISULA for rectangular grids, report Z81. Delft Hydraulics. Prepared for Ministerie van Verkeer en Waterstaat Rijkswaterstaat,

Dienst Getijdewateren (RWS, DGW) 169 (56), Z162. https://puc.overheid.nl/rijkswa terstaat/doc/PUC_96984_31/.

Wang, Z.B., Winterwerp, J.C., He, Q., 2014. Interaction between suspended sediment and tidal amplification in the Guadalquivir Estuary. Ocean Dynam. 64, 1487–1498. https://doi.org/10.1007/s10236-014-0758-x.

Webb, D.J., 1973. On the age of semi-diurnal tide. Deep-Sea Res. Oceanogr. Abstr. 20, 847–852. https://doi.org/10.1016/0011-7471(73)90006-5.